PAPER

Check for updates

Highly luminescent dual-phase CsPbBr$_3$/Cs$_4$PbBr$_6$ microcrystals for a wide color gamut for backlight displays†

V. Naresh,*[a] Taehyung Jang,[b] Yoonsoo Pang [iD] [b] and Nohyun Lee*[a]

Cesium lead bromide perovskite nanocrystals (NCs) embedded in Cs$_4$PbBr$_6$ or CsPb$_2$Br$_5$ matrices forming core/shell structures are promising luminescent materials that exhibit remarkable photoluminescence properties meeting the need in a wide range of applications while overcoming stability challenges. Here, we report the large-scale, ligand-free synthesis of dual-phase Cs$_4$PbBr$_6$/CsPbBr$_3$ microcrystals (MCs) using ultrasonication at room temperature, exhibiting a high photoluminescence quantum yield (PLQY) of 82.7% and good stability. High-resolution transmission electron microscopy and X-ray photoelectron characterization confirm that CsPbBr$_3$ NCs are embedded in the Cs$_4$PbBr$_6$ matrix-forming CsPbBr$_3$/Cs$_4$PbBr$_6$ dual-phase structure. The evolution of the luminescence properties with temperature suggests that the strong green emission results from direct exciton recombination in the isolated [PbBr$_6$]$^{4-}$ octahedra, which possess a large exciton binding energy of 283.6 meV. As revealed from their emission intensities, the dual-phase CsPbBr$_3$/Cs$_4$PbBr$_6$ MCs demonstrate excellent stability against ultraviolet irradiation (76%), good moisture resistance (42.7%), and good thermal tolerance (51%). It is understood that such excellent PLQY and stability are due to the surface passivation of the CsPbBr$_3$ NCs attributed to the large bandgap as well as the isolated [PbBr$_6$]$^{4-}$ octahedra separated by Cs$^+$ ions in the Cs$_4$PbBr$_6$ crystal lattice. Finally, the suitability of the green-emitting CsPbBr$_3$/Cs$_4$PbBr$_6$ material for achieving white-light emission and a wide color gamut is evaluated by constructing a prototype white light-emitting diode (w-LED) using CsPbBr$_3$/Cs$_4$PbBr$_6$ and red-emitting K$_2$SiF$_6$:Mn^{4+} materials taken in different weight ratios and combined with a blue light-emitting InGaN LED chip (λ = 455 nm). The constructed w-LED device exhibits the color coordinates (0.3315, 0.3289), an efficacy of 68 lm W^{-1}, a color rendering index of 87%, a color temperature of 5564 K, and a wide color gamut of ~118.78% (NTSC) and ~88.69% (Rec. 2020) with RGB color filters in the CIE 1931 color space. Therefore, based on our present findings, we strongly believe that the dual-phase CsPbBr$_3$/Cs$_4$PbBr$_6$ material is a promising green-emitting phosphor for use in w-LEDs as the backlight of display systems.

Introduction

All-inorganic PNCs (CsPbX$_3$, X = Cl, Br, and I) have gained consideration attention due to their narrow emission bandwidth and tunable bandgap, high-defect tolerance, large absorption cross-section, and near-unity photoluminescence quantum yield (PLQY),[1-3] which have enabled them to be used in a variety of promising applications, including color conversion and electroluminescent materials in light-emitting and display devices,[4] photovoltaics,[5] laser gain media, and X-ray scintillating materials,[6] and for anti-counterfeiting applications.[7] Despite their unique optical and photophysical properties, CsPbX$_3$ materials suffer from structural instability when exposed to ultraviolet (UV) radiation, moisture, and heat. They are affected by their inherent phase transformation when directly used in practical applications, such as white light-emitting devices. Additionally, their unsuitability for large-scale industrial synthesis requirements is another setback. To circumvent these challenges, several approaches have been proposed, such as encapsulation in inorganic shells, including ZnS,[8] CdS,[9] TiO$_2$,[10] Al$_2$O$_3$,[11] PbSO$_4$,[12] and mesoporous silica,[13] and embedding in polymer[14] and glass[15] matrices as well as heteroepitaxial structures, including CsPbBr$_3$/Cs$_4$PbBr$_6$ [16] and CsPbBr$_3$/CsPb$_2$Br$_5$ core/shell structures.[17] Nevertheless, since these integration and incorporation methods are expensive,

[a]*School of Advanced Materials Engineering, Kookmin University, Seoul 02707, Republic of Korea. E-mail: naresh17@kookmin.ac.kr, nohyunlee@kookmin.ac.kr*
[b]*Department of Chemistry, Gwangju Institute of Science and Technology, 123 Cheomdangwagi-ro, Gwangju 61005, Republic of Korea*
†Electronic supplementary information (ESI) available. See DOI: https://doi.org/10.1039/d2nr05653d

labor-intensive, and complex, they can only be performed in the laboratory and are difficult for synthesis and optimization for large-scale production. Therefore, these challenges have triggered an extensive exploration for highly luminescent $CsPbX_3$-related structures that are structurally stable in different environments, such as two-dimensional (2D; $CsPb_2X_5$) and zero-dimensional (0D; Cs_4PbX_6) perovskites.[18–20]

$CsPbBr_3$ has a three-dimensional (3D) structure characterized by corner-sharing $[PbBr_6]^{4-}$ octahedra with Cs^+ cations filling the spaces created by four neighboring $[PbBr_6]^{4-}$ octahedra.[21] Although the $CsPbBr_3$ material has been extensively explored from an application perspective, its structural instability has been a hindrance. Unlike the 3D $CsPbBr_3$ structure, the $[PbBr_6]^{4-}$ octahedra are decoupled from the halide ions, without sharing any corners or edges and are surrounded by isolated Cs^+ cations in the 0D Cs_4PbBr_6 structure.[21,22] The unique 0D structure characterized by decoupled $[PbBr_6]^{4-}$ octahedra displays significant quantum confinement and exciton–phonon interactions, which lead to exciton localization, self-trapping, polaron generation, and intrinsic Pb^{2+} ion emission.[22,23] Due to their stability and photoluminescence (PL) capabilities, 0D Cs_4PbBr_6 perovskite materials have attracted exceptional interest from the scientific community over the last decade as green phosphors for realizing white-light emission.[20,21] However, the origin of the strong green luminescence remains a subject of debate. Several research groups have demonstrated possible luminescence mechanisms for the intense green PL from Cs_4PbBr_6, which include (i) emission from $CsPbBr_3$ NCs (as impurities, inclusions, or $CsPbBr_3/Cs_4PbBr_6$ interfaces) and (ii) defect-induced emission (such as Br vacancies, interstitial hydroxyl, polybromide, and self-trapped excitation).[22–30] The absence of traces related to $CsPbBr_3$ NC impurities in the X-ray diffraction (XRD) pattern, transmission electron microscopy (TEM) images, and scanning electron microscopy (SEM) images has prompted concerns regarding the accuracy of the former theory. Although the latter theory is supported by density functional theory (DFT) simulations, it faces the problem of reproducing the calculated deep-level defect states through other DFT simulations and rarely agrees with the experimental results obtained for lead halide perovskites.[30] However, many research groups have provided credible and compelling evidence for the green luminescence being caused by the presence of $CsPbBr_3$ NCs as an impurity in the Cs_4PbBr_6 structure. Zou et al. conducted high-pressure experiments and DFT calculations to demonstrate that the green luminescence in Cs_4PbBr_6 originates from the $CsPbBr_3$ impurities embedded in it.[31] Bao et al. identified the presence of $CsPbBr_3$ NCs in emissive Cs_4PbBr_6 using correlated Raman–PL measurements as a passive structure–property method.[32] Riesen et al. employed a cathodoluminescence imaging technique to demonstrate the presence of low impurity levels of $CsPbBr_3$ in Cs_4PbBr_6 synthesized mechanochemically through ball milling.[33] Zhong et al. reported that centimeter-sized Cs_4PbBr_6 crystals with embedded $CsPbBr_3$ NCs exhibited superior green luminescence.[34]

To date, all-inorganic PNCs have been synthesized using chemical vapor deposition (CVD) and solution-based synthesis methods like hot-injection, solvothermal methods, room temperature-based ligand-mediated precipitation and super-saturated recrystallization.[35] The hot-injection method has been widely used to synthesize PNCs; however, it is expensive and time-consuming, and requires certain reaction conditions to synthesize PNCs, such as high temperature, vacuum, inert atmospheres, and pre-synthesized precursors, resulting in limited yield and repeatability. To synthesize PNCs using room temperature-based approaches, the precursors must be mixed with large quantities of polar solvents, such as dimethyl sulfoxide (DMSO) and N,N-dimethylformamide (DMF), followed by treatment with nonpolar solvents, such as toluene or hexane. Despite the high yield of PNCs obtained using these approaches, they are sensitive to polar solvents, resulting in the formation of defects.[35,36] Therefore, considering these above shortcomings to produce PNCs with high quality and excellent stability, ultrasonication-assisted synthesis is considered to be a promising method due to factors such as a rapid reaction rate, controllable reaction conditions, quality and quantity of the yield, less labor-intensive synthesis processes, optimization for large-scale production, low cost and safety.[34,37,38] The ultrasonication method is widely used to synthesize high-quality nano- and micro-sized particles on a large scale. In contrast to the hot-injection method,[1] precursors do not have to be pre-treated or degassed before the reaction occurs. Instead, ultrasonication allows the reaction to occur in an ambient environment. Additionally, it accelerates the nucleation and growth of NCs and can reduce the reaction time.

Herein, we present a facile and eco-friendly ultrasonication approach for the large-scale synthesis of ligand-free lead halide perovskite (LHP) MCs at room temperature. We demonstrated that this approach could generate both single-phase ($CsPbBr_3$, Cs_4PbBr_6) and dual-phase ($CsPbBr_3/Cs_4PbBr_6$) MCs at a rapid pace by varying the precursor ($CsBr$, $PbBr_2$) content in mixed solvents of DMF and DMSO taken in low quantities (Fig. 1). Our investigation sheds light on the phase transitions between the Cs–Pb–Br compounds, their formation kinetics at different stages, and microstructure. DMF and DMSO have an effect on the solubility of $CsBr$ and $PbBr_2$ in the solvent as they can control the growth of dual-phase $CsPbBr_3/Cs_4PbBr_6$ MCs precisely. We also discussed the role of the dual-phase formation in generating green emission, which is caused by the presence of $CsPbBr_3$ NCs as an impurity in the Cs_4PbBr_6 structure. Additionally, this facile synthesis method reduces the reaction time and production cost. The MCs synthesized through this approach exhibit a high PLQY without using antisolvents, such as toluene and chloroform. Considering the high PLQY and stability of green-emitting dual-phase $CsPbBr_3/Cs_4PbBr_6$ microcrystals (MCs), we developed a prototype white LED (w-LED) using optimized contents of the as-synthesized dual-phase $CsPbBr_3/Cs_4PbBr_6$ MCs with $K_2SiF_6:Mn^{4+}$ ($\lambda = 628$ nm) phosphors coupled to a blue light-emitting InGaN LED chip ($\lambda = 455$ nm).
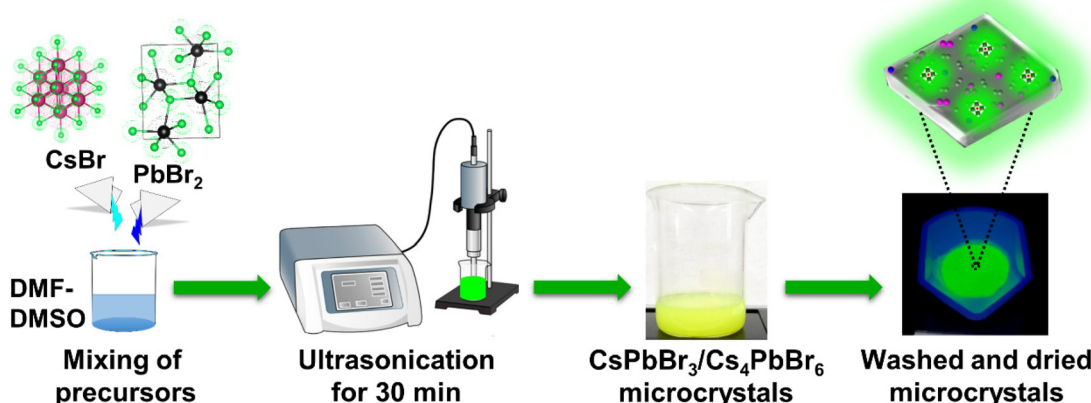
Fig. 1 Scheme for the synthesis of dual-phase $CsPbBr_3/Cs_4PbBr_6$ MCs using ultrasonication process.

Results and discussion

As shown in Fig. 1, the synthesis of the dual-phase $CsPbBr_3/$ Cs_4PbBr_6 MCs involves a single step at room temperature. $CsBr : PbBr_2$ was taken in various molar ratios and ultrasonicated in a 1 : 1 ratio of DMF and DMSO to synthesize the dual-phase MCs. Due to the different solubilities of precursors in DMF and DMSO, initially $CsPbBr_3$, then Cs_4PbBr_6, and finally, dual-phase $CsPbBr_3/Cs_4PbBr_6$ MCs with a lemon-yellow color are formed at different reaction times. The sample was centrifuged, and the precipitate was dried at 70 °C to obtain the dual-phase $CsPbBr_3/Cs_4PbBr_6$ MCs. The details of the synthesis methodology of the dual-phase $CsPbBr_3/Cs_4PbBr_6$ MCs depending on the ultrasonication time are described in the Experimental section provided in the ESI.†

The XRD pattern of the Cs_4PbBr_6 microcrystals (MCs) synthesized with the assistance of ultrasonication for 30 min, shown in Fig. 2a, exhibits strong diffraction peaks, which can be well indexed to the rhombohedral crystal structure (JCPDS# 73-2478) with the $R\bar{3}c$ (167) phase group, lattice parameters $a = b = 13.73$ Å and $c = 17.31$ Å, and corresponding angles $\alpha = \beta = 90°$ and $\gamma = 120°$. In addition, no diffraction peaks attributed to $CsPbBr_3$ are noticed in the XRD pattern of the synthesized powder. Transmission electron microscopy (TEM) images of the samples synthesized at 3, 10 and 30 min are shown in Fig. S1a, b† and Fig. 2b, to understand the evolution of morphology based on time. The sample synthesized at 3 min exhibited micrometer sized cube-like $CsPbBr_3$ structure seen in Fig. S1a,† and on further increasing the reaction time to 10 min, the particle shape was transformed to soft edges exhibiting the $CsPbBr_3/Cs_4PbBr_6$ matrix shown in Fig. S1b† (inset shows the corresponding high-resolution TEM (HR-TEM) images). Further increasing of the reaction time to 30 min resulted in rhombohedral particles with sharp edges as shown in Fig. 2b. As shown in Fig. 2c, a large number of small particles with an average diameter of 10.28 nm are embedded on the edges and outer surface of the Cs_4PbBr_6 material. This suggests the formation of the dual-phase $CsPbBr_3/Cs_4PbBr_6$
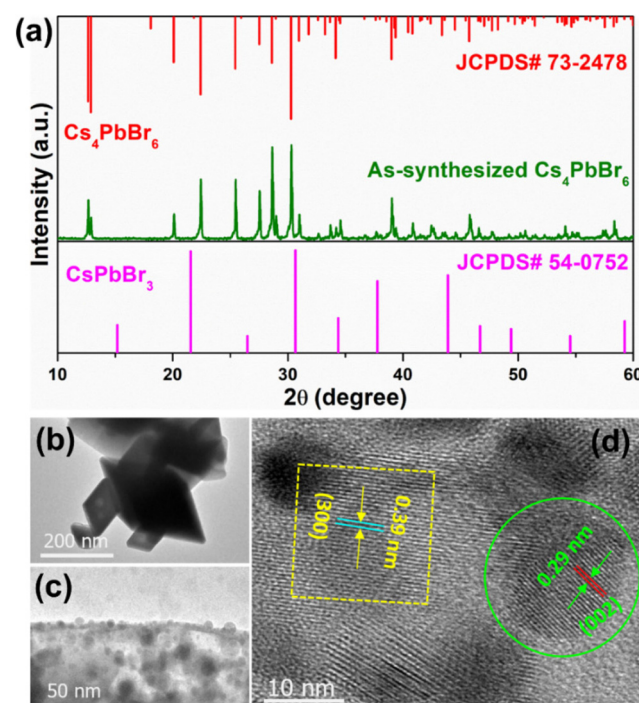

Fig. 2 (a) Powder XRD pattern of the Cs_4PbBr_6 microcrystals (MCs), (b and c) TEM and (d) HR-TEM images of the Cs_4PbBr_6 MCs embedded with $CsPbBr_3$ nanocrystals (NCs).

MC structure, which is similar to the previously reported TEM results for the Cs_4PbBr_6 material.[39–41] The crystal lattice of Cs_4PbBr_6 comprises closely packed anions with cations fixed at the interstitial positions; the smaller ionic radius of Pb^{2+} (119 pm) compared with those of Cs^+ (169 pm) and Br^- (195 pm), as well as the existence of ionic dislocation and displacement, is beneficial for the embedding of the $CsPbBr_3$ NCs into the Cs_4PbBr_6 MCs. Therefore, a high-resolution TEM (HR-TEM) image was acquired to identify the coexistence of these phases. Fig. 2d shows a HR-TEM image exhibiting two

Paper

different sets of lattice fringes, which can be attributed to the $CsPbBr_3$ and Cs_4PbBr_6 phases. The region circled in green in Fig. 2d exhibited a lattice spacing of 0.29 nm, which is consistent with the (002) crystal plane, confirming the monoclinic $CsPbBr_3$ structure. The region inside the yellow square in Fig. 2d exhibits a lattice spacing of 0.39 nm, corresponding to the (113) crystal plane, confirming the rhombohedral Cs_4PbBr_6 structure. Therefore, the HR-TEM results demonstrate that $CsPbBr_3$ NCs are incorporated into the solid-rhombohedral prism of the Cs_4PbBr_6 structure, forming dual-phase $CsPbBr_3/Cs_4PbBr_6$ MCs. The dual-phase $CsPbBr_3/Cs_4PbBr_6$ MCs have a rhombohedral shape with a smooth outer surface and almost sharp edges, as shown in the low- and high-magnification field-emission scanning electron microscopy (FE-SEM) images (Fig. S2a and b†). The element mapping (cesium (Cs) in green, lead (Pb) in blue, and bromide (Br) in yellow) (Fig. S2c–f†) and energy-dispersive spectroscopy (EDS) profiles (Fig. S2g†) confirm the presence of Cs, Pb, and Br elements in the dual-phase MCs, with atomic percentages of 35.45%, 9.68%, and 54.87%, respectively. The molar ratio of $CsPbBr_3$ to Cs_4PbBr_6 is determined to be approximately 1 : 8. Moreover, the EDS maps provide the homogeneous distribution of the elements in the dual-phase MCs, represented by colored dots.

The X-ray photoelectron spectroscopy (XPS) measurement was performed for the pure $CsPbBr_3$, dual-phase $CsPbBr_3/Cs_4PbBr_6$, and pure Cs_4PbBr_6 MCs to quantify the number of elements as well as characterize their chemical states, chemical shifts, and the bonding between them. Fig. 3a shows the wide-scan XPS profiles of the emissive $CsPbBr_3$, dual-phase $CsPbBr_3/Cs_4PbBr_6$, and non-emissive Cs_4PbBr_6 MCs exhibiting the presence of Cs 3d, Pb 4f, and Br 3d peaks in the synthesized materials.

The high-resolution (HR) core-level spectra of the Cs 3d, Pb 4f, and Br 3d orbitals are shown in Fig. S3a, b,† and Fig. 3b. The HR-XPS spectra of the Cs 3d and Pb 4f orbitals of the three materials displayed two distinct peaks assigned to $3d_{5/2}$, $3d_{3/2}$, and $4f_{5/2}$, $4f_{7/2}$, respectively, due to the spin–orbit splitting. The $CsPbBr_3/Cs_4PbBr_6$ XPS peaks are shifted to the higher binding energies (BEs) compared to $CsPbBr_3$ and Cs_4PbBr_6, indicating lower electron density (Fig. S3a and b†).
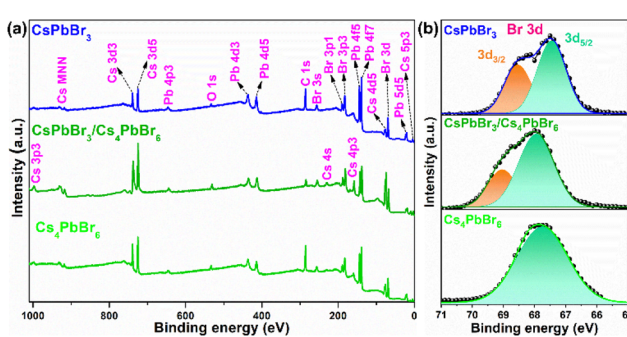
Fig. 3b shows the deconvoluted Gaussian fitting of the HR-XPS profiles of Br 3d orbitals for emissive $CsPbBr_3$, dual-phase $CsPbBr_3/Cs_4PbBr_6$, and non-emissive Cs_4PbBr_6. The Br 3d peak of Cs_4PbBr_6 exhibited a single broad peak with a BE of 67.86 eV, which is consistent with a previous report,[34] while the Br 3d peaks of $CsPbBr_3$ and $CsPbBr_3/Cs_4PbBr_6$ exhibited two peaks, which are assigned to the $3d_{5/2}$ and $3d_{3/2}$ doublets due to the spin–orbit splitting. The doublets with BEs of 67.43 and 68.54 eV for $CsPbBr_3$ and 67.93 and 69.03 eV for $CsPbBr_3/Cs_4PbBr_6$ are attributed to the $3d_{5/2}$ and $3d_{3/2}$ components, respectively, of the Br atoms in the interior and on the outer surface. Interestingly, from Fig. 3b, we noticed that the Gaussian peak with a BE of 67.93 eV of $CsPbBr_3/Cs_4PbBr_6$ lies very much close to 67.86 eV of Cs_4PbBr_6 corresponding to the Br atoms in the isolated $[PbBr_6]^{4-}$ units of Cs_4PbBr_6 MCs.[42] The Gaussian peak at 69.03 eV of $CsPbBr_3/Cs_4PbBr_6$, which is close to 68.54 eV of $CsPbBr_3$, corresponds to the Br atoms of the CsBr impurities or corner-sharing $[PbBr_6]^{4-}$ octahedra of $CsPbBr_3$ when the $CsPbBr_3$ NCs are present in the green color-emitting MCs.[34,43] Therefore, the XPS analysis supports the existence of a small quantity of $CsPbBr_3$ impurities in the Cs_4PbBr_6 MCs. The Cs : Pb : Br compositional ratio determined from the XPS measurements is consistent with the EDS result. Therefore, based on the HR-TEM and XPS results, it is evident that small impurities of $CsPbBr_3$ NCs are present in Cs_4PbBr_6 forming a dual-phase $CsPbBr_3/Cs_4PbBr_6$ microstructure.

Considering the structural results, we initially explored the effect of the $CsBr : PbBr_2$ molar ratio on the structure and optical properties of the dual-phase $CsPbBr_3/Cs_4PbBr_6$ MCs by performing XRD, absorption, and PL measurements for different $CsBr : PbBr_2$ molar ratios (1 : 1, 2 : 1, 4 : 1, and 6 : 1) in a mixed solution of DMF–DMSO. For a $CsBr : PbBr_2$ ratio of 1 : 1, the $CsPbBr_3$ peaks observed in the XRD pattern (Fig. S4a†) can be well indexed to the JCPDS# 18-0364 standard card (monoclinic $CsPbBr_3$), and the strong absorption onset in the green region (Fig. S4b†) suggests the formation of the $CsPbBr_3$ structure. However, no emission is observed under UV excitation (Fig. S4c†), indicating the bulk nature of the formed compound.[7,44] Therefore, as the $CsBr : PbBr_2$ molar ratio is increased to 2 : 1, diffraction peaks attributed to Cs_4PbBr_6 are noticed alongside the $CsPbBr_3$ diffraction peaks, suggesting $CsPbBr_3$ phase transformation to Cs_4PbBr_6 with excess CsBr. Furthermore, the sample displays a moderately strong band at 315 nm in the UV region and a strong onset absorption at 528 nm with weak green luminescence under UV light. As the $CsBr : PbBr_2$ molar ratio is increased to 4 : 1, no traces of $CsPbBr_3$ are noticed in the XRD pattern (Fig. S4a†). Moreover, the appearance of a strong band at 315 nm and a weak onset at 528 nm in the absorption spectrum suggests the presence of small traces of $CsPbBr_3$ in the Cs_4PbBr_6 structure (Fig. S4b†). The appearance of intense green luminescence under UV excitation (Fig. S4c†) confirms the formation of the dual-phase $CsPbBr_3/Cs_4PbBr_6$ MCs. Therefore, considering this outcome, the $CsBr : PbBr_2$ molar ratio was further increased to 6 : 1. In this case, the XRD pattern (Fig. S4a†) shows no impurity peaks related to $CsPbBr_3$; however, an

Fig. 3 (a) Wide-scan X-ray photoelectron spectrum of emissive $CsPbBr_3$, dual-phase $CsPbBr_3/Cs_4PbBr_6$ and non-emissive Cs_4PbBr_6. (b) High-resolution X-ray photoelectron spectra of Br (3d).

impurity peak attributable to CsBr (JCPDS# 05-0588) is noticed at θ = 29.5°, which could be due to the excessive CsBr loading. The absorption spectrum displays a strong band at 315 nm and a further weakened onset at 528 nm in the absorption spectrum, suggesting that small traces of $CsPbBr_3$ are still present in the Cs_4PbBr_6 structure (Fig. S4b†). The PL spectrum displays a slightly less intense green emission spectrum than that observed for the 4 : 1 molar ratio (Fig. S4c†). The emission intensity increases until the $CsBr : PbBr_2$ molar ratio is 4 : 1, above which a slight decrease in the emission intensity is noticed in the PL spectrum, which could be attributed to the low Pb^{2+} concentration. The photographs of the sample synthesized at different $CsBr : PbBr_2$ molar ratios (=1 : 1, 2 : 1, 4 : 1, and 6 : 1) under day and UV light are shown in Fig. S4d.†

Furthermore, to better understand the formation of the dual-phase $CsPbBr_3/Cs_4PbBr_6$ MCs, CsBr and $PbBr_2$ in a molar ratio of 0.4 : 0.1 were placed in a vial, and DMF (0.5 ml) and DMSO (0.5 ml) solutions were added for the ultrasonication treatment. Fig. 4a shows the photographs of the ultrasonication process and the as-synthesized samples under daylight and UV light. CsBr is insoluble in DMF, whereas the solubility of $PbBr_2$ is higher even at room temperature; as a result,

the formation of $CsPbBr_3$ is accelerated. Since CsBr dissolves easily in DMSO, it induces a higher concentration of Cs^+ ions, which is beneficial for accelerating the phase transformation from $CsPbBr_3$ to Cs_4PbBr_6 during the synthesis of the dual-phase $CsPbBr_3/Cs_4PbBr_6$ MCs.[44,45] Here, we investigated the different intermediate steps involved in the formation of the dual-phase $CsPbBr_3/Cs_4PbBr_6$ MCs because the color change in the precursor salts depends on the ultrasonication time. The formation of the dual-phase $CsPbBr_3/Cs_4PbBr_6$ MCs with the assistance of ultrasonication occurs in four stages: (i) interfacial conversion, (ii) formation of orange-colored $CsPbBr_3$ MCs, (iii) formation of white-colored Cs_4PbBr_6 MCs, and (iv) formation of lemon-yellow colored dual-phase $CsPbBr_3/Cs_4PbBr_6$ MCs. The photographs of the products exhibiting different colors at different stages (time intervals t = 0, 3, 10, and 30 min) during ultrasonication are shown in Fig. 4b–e, and changes in their structure are identified from the corresponding XRD patterns (Fig. 4f). In the first stage (Fig. 4b), when the DMF–DMSO solution is added to the CsBr and $PbBr_2$ precursor salts, a $CsPbBr_3$ (orange color) layer is immediately formed through the interfacial conversion of the undissolved salts on the surface. In the second stage (Fig. 4c), when the
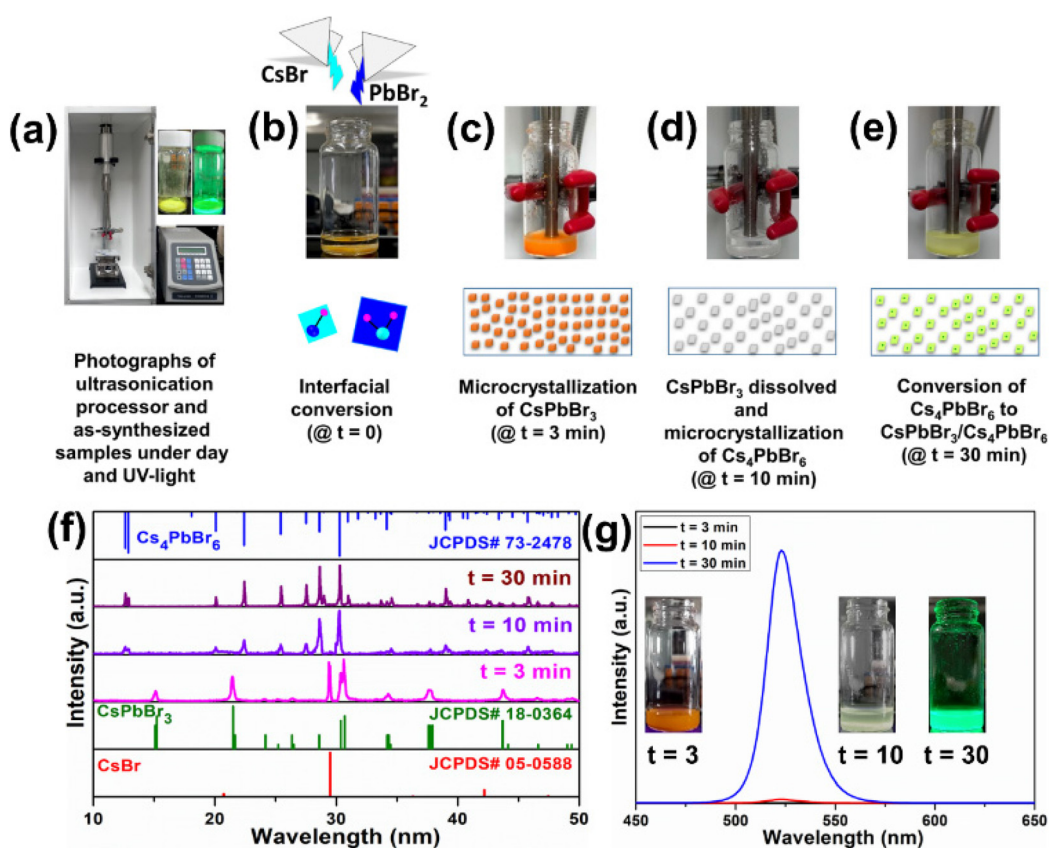
Fig. 4 (a) The photographs of the ultrasonication processor and as-synthesized samples taken during day and under UV light. Time-dependent changes in the precursors (CsBr, and $PbBr_2$) during the ultrasonication process and the formation mechanism of dual-phase $CsPbBr_3/Cs_4PbBr_6$ microcrystals at different reaction time intervals (b) t = 0 min, (c) t = 3 min, (d) t = 10 min, and (e) t = 30 min, (f) XRD profiles of the final products at different reaction time intervals t = 3, 10, and 30 min indexed to JCPDS# 05-0588 (CsBr), JCPDS# 18-0364 ($CsPbBr_3$), and JCPDS# 73-2478 (Cs_4PbBr_6), and (g) PL profiles of the obtained products at t = 3, 10, and 30 min (inset photographs of their luminescence under UV light).

salts are ultrasonicated for 3 min, the reactants form an intermediate compound, *i.e.*, a Pb-rich phase of $CsPbBr_3$ (orange color) in the clear DMF–DMSO solution. The spontaneous nucleation and growth of $CsPbBr_3$ occur because of the higher concentration of Pb^{2+} than Cs^+ in the solution due to the low solubility of CsBr in DMF. $Cs^+ + Pb^{2+} + 3Br^- \rightarrow CsPbBr_3$ is the crystallization reaction. The XRD analysis of the orange product shows that the diffraction peaks agree well with the JCPDS# 18-0364 standard card. This shows that the structure of the orange product is monoclinic $CsPbBr_3$ (Fig. 4f). However, an impurity peak at around 29.5° that can be attributed to CsBr (JCPDS# 05-0588) is noticed due to the undissolved CsBr. The third stage (Fig. 4d) is governed by the dissolution–crystallization mechanism; when the reactants are ultrasonicated for 10 min, with the depletion of Pb^{2+} (*i.e.*, $PbBr_2$), the gradual dissolution of Cs^+ (CsBr) occurs in the DMF–DMSO solution. During this crystallization process, the reactive amount of Cs^+ is larger than that of Pb^{2+}, which contributes to the Cs^+-rich reaction condition. Due to the high solubility of the $CsPbBr_3$ crystals in DMSO, they begin to dissolve and react with CsBr, resulting in the Cs_4PbBr_6 MCs (white). The crystallization and dissolution processes are described by the following equations: $4Cs^+ + Pb^{2+} + 6Br^- \rightarrow Cs_4PbBr_6$, and $CsPbBr_3 \rightarrow Cs^+ + Pb^{2+} + 3Br^-$, respectively. The XRD pattern of the white-colored product obtained after ultrasonication for 30 min is in good agreement with the JCPDS# 73-2478 standard card, which corresponds to the Cs_4PbBr_6 structure. However, small impurity peaks attributed to CsBr and $CsPbBr_3$ are present in the XRD pattern of the white product (Fig. 4f). In the fourth stage (10–30 min ultrasonication) (Fig. 4e), the Cs_4PbBr_6 matrix grows on the surface of the $CsPbBr_3$ NCs, which are produced at this stage. The XRD pattern of the product with lemon yellow color obtained after ultrasonication for 30 min matches well with the JCPDS# 73-2478 standard card, which corresponds to the rhombohedral Cs_4PbBr_6 structure. However, no peaks attributable to $CsPbBr_3$ are present in the XRD pattern of the final product (Fig. 4f). The dual-phase $CsPbBr_3/Cs_4PbBr_6$ MCs are generated by the ripening of the $CsPbBr_3/Cs_4PbBr_6$ matrix (lemon-yellow color). The PL trends were also recorded for the products at time intervals of t = 3, 10, and 30 min (Fig. 4f), and their photographs under UV light are shown in Fig. 4g. After 3 min of the ultrasonication process, the products do not show emission under UV excitation. After 10 min, the products exhibit very weak emission under UV excitation, which indicates the initial stage of the formation of $CsPbBr_3$ within the Cs_4PbBr_6 microstructure. After 30 min of ultrasonication, the products yield an intense green emission under UV light, suggesting the formation of a stable dual-phase $CsPbBr_3/Cs_4PbBr_6$ microstructure.

To gain a clear insight into the photophysical properties of the dual-phase $CsPbBr_3/Cs_4PbBr_6$ MCs prepared using the ultrasonication process, the photophysical properties of the $CsPbBr_3/Cs_4PbBr_6$ were compared with those of the pure Cs_4PbBr_6 and $CsPbBr_3$ NCs (Fig. 5a–c) synthesized *via* the hot-injection method. The pure Cs_4PbBr_6 NCs display a strong absorption peak in the deep-UV region at around 315 nm,
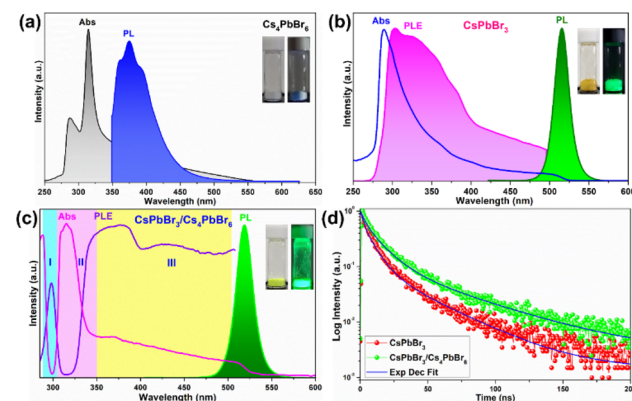

Fig. 5 (a) Absorption and photoluminescence spectra of pure Cs_4PbBr_6, (b) absorption, photoluminescence, and excitation spectra of pure $CsPbBr_3$, (c) absorption, photoluminescence, and excitation spectra of dual-phase $CsPbBr_3/Cs_4PbBr_6$, and (d) time-resolved photoluminescence decay curves of $CsPbBr_3$, and $CsPbBr_3/Cs_4PbBr_6$ at λ_{exci} = 365 nm.

which is assigned to the $^1S_0 \rightarrow {}^3P_1$ transition, and the PL spectrum exhibits a broad band in the range of 350–520 nm, with a peak maximum at around 372 nm, which is assigned to the $Pb^{2+}:{}^3P_1 \rightarrow {}^1S_0$ transition in the isolated $[PbBr_6]^{4-}$ octahedral units in Cs_4PbBr_6.[46] However, no emission occurs in the green region (Fig. 5a). The $CsPbBr_3$ NCs exhibits an absorption band edge at 505 nm with an optical bandgap of 3.44 eV and a strong PL band at 514 nm (Fig. 5b). The optical absorption, PL excitation (PLE), and PL bands of the emissive Cs_4PbBr_6 MCs are shown in Fig. 5c. The optical absorption spectrum is composed of a couple of absorption bands, one at 315 nm in the UV region (which corresponds to the absorption band of pure Cs_4PbBr_6) and the other one located at 510 nm in the green region (which corresponds to the absorption band of pure $CsPbBr_3$). The strong peak at 315 nm is due to the optical transitions between the localized states within the decoupled $[PbBr_6]^{4-}$ octahedral units of Cs_4PbBr_6 (*i.e.*, it arises from the $^1S_0 \rightarrow {}^3P_1$ transition of the Pb^{2+} centers).[40,46] The other band at 510 nm matches the band at 505 nm of $CsPbBr_3$. Additionally, a strong PL band is observed at around 522 nm, which is similar to that of $CsPbBr_3$ (@514 nm) and is absent in the case of pure Cs_4PbBr_6. The small red-shift in the absorption and PL spectra of dual-phase $CsPbBr_3/Cs_4PbBr_6$ MCs but not in those of $CsPbBr_3$ is attributed to the quantum size effect caused by the increase of the particle size.[47,48] It is noteworthy to mention that, shell growth reduces the amount of surface dangling bonds, which enhances fluorescence intensity; however, this does not always result in a blue shift of the luminescence.[49,50] Furthermore, the overlap between the absorption spectrum of the pure Cs_4PbBr_6 and the PL spectrum of $CsPbBr_3$ provides evidence for the possibility of energy transfer from Cs_4PbBr_6 to $CsPbBr_3$ in the dual-phase $CsPbBr_3/Cs_4PbBr_6$ MCs (Fig. S5a†). Therefore, upon monitoring the $CsPbBr_3/Cs_4PbBr_6$ with $CsPbBr_3$ emission, the resultant PLE spectrum exhibits excitation features of pure Cs_4PbBr_6 and

Pb^{2+} ions. This indicates that the green PL observed in the dual-phase $CsPbBr_3/Cs_4PbBr_6$ MCs is due to the embedded $CsPbBr_3$ NCs (Fig. S5b†). The above results show that the green PL and absorption bands observed in the dual-phase $CsPbBr_3/Cs_4PbBr_6$ MCs originate from the coexistence of the Cs_4PbBr_6 and $CsPbBr_3$ structures.

The above speculation is further supported by analyzing the absorption and PLE spectra of $CsPbBr_3/Cs_4PbBr_6$ (Fig. 5c). For this purpose, the absorption spectrum is classified into three regions labelled as I, II, and III. In the absorption spectrum, regions I and II represent the intrinsic absorption of Cs_4PbBr_6 in the absorption spectrum, while region III necessitates further clarification because it deviates from the Urbach tail.[51,52] However, the steep absorption in region II suggests that the mid-bandgap states are suppressed in Cs_4PbBr_6. Despite this, the sample still exhibits a noticeable absorption onset in the green region, which appears too strong to be caused by the suppressed intraband states, as shown in the figure (Fig. 5c). Based on this finding, the origin of the bright green luminescence can be decoupled from the intraband defect states. Furthermore, the absorption and emission spectra trends are consistent with each other in region III; they display enhanced absorption, which leads to an intensified PLE signal. In contrast to region III, the absorption and PLE signals in regions I and II are symmetric approximately at the same wavelengths (~297 nm and ~315 nm), displaying a weakened absorption, which results in an enhanced PLE signal. The dip in the absorption signals indicates the absence of states to accommodate electrons in Cs_4PbBr_6. Therefore, when Cs_4PbBr_6 is excited with photons in this region, the PL intensity remains the same due to weak absorption; however, a sharp green PL is observed in the green region, contradicting the above conjecture. Furthermore, the characteristic sharp absorption onset at around 510 nm in the dual-phase $CsPbBr_3/Cs_4PbBr_6$ MCs (Fig. 5c) contradicts the long Urbach tail reported by Wang et al., ruling out the possibility that the green PL originates from intraband defect-states of the Br vacancies.[23] Moreover, the band edge located at 510 nm in $CsPbBr_3/Cs_4PbBr_6$ suggests a direct exciton recombination PL. If defect-related states exist in the gap between the valence and conduction bands, they will capture the electrons from the conduction band and generate defect-related emissions. The fact that the emission band measured in the range of 450–650 nm under different excitation wavelengths in the range of 350–500 nm (Fig. S6†) is independent of position and shape implies the absence of defect-related emitting states in the synthesized MCs. Therefore, the absorption and PLE analyses support the theory of the green PL originating from small $CsPbBr_3$ impurities embedded in Cs_4PbBr_6. These photophysical properties confirm that $CsPbBr_3$ NCs impurities are present in the Cs_4PbBr_6 MCs, enabling them to exhibit a strong green luminescence. Fig. 5d shows the time-resolved PL spectra of the $CsPbBr_3$ and fits the time-resolved PL profiles:

$$I(t) = A_1 \exp\left(-\frac{t}{\tau_1}\right) + A_2 \exp\left(-\frac{t}{\tau_2}\right),$$

where I is the PL intensity at time (t), τ_1 and τ_2 are the short (fast) and long (slow) decay component lifetimes, respectively, and A_1 and A_2 are the amplitudes (fitting parameters). The average lifetime is evaluated from $\tau_{avg} = (A_1\tau_1^2 + A_2\tau_2^2)/(A_1\tau_1 + A_2\tau_2)$ (Table S1†). The bi-exponential fitting gives a short (τ_1) lifetime of 6.47 ns and a longer (τ_2) lifetime of 31.31 ns. Since the dual-phase $CsPbBr_3/Cs_4PbBr_6$ behaves as a core/shell material, from the decay components presented in Table S1,† the shorter (τ_1) decay component, which can be attributed to interior $CsPbBr_3$ state recombination, and the longer (τ_2) decay component, which can be attributed to surface defects radiative recombination (surface passivation of $CsPbBr_3$ NCs) can be understood.[40,43] The contribution of the short (τ_1) and long (τ_2) components to the total emission decay profile was calculated using the amplitudes A_1 and A_2 for the dual-phase $CsPbBr_3/Cs_4PbBr_6$ MCs. The contribution percentage of a shorter lifetime (τ_1) accounts for nearly 45.8% and the longer lifetime (τ_2) accounts for nearly 54.1% of the total emission decay. Taking the amplitudes into consideration (Table S1†), the value of amplitude A_1 corresponding to τ_1 of $CsPbBr_3$ is larger than that of $CsPbBr_3/Cs_4PbBr_6$ and the value of amplitude A_2 corresponding to τ_2 of $CsPbBr_3$ is smaller than that of $CsPbBr_3/Cs_4PbBr_6$, suggesting that the surface defects of $CsPbBr_3$ are well passivated by Cs_4PbBr_6. The dual-phase $CsPbBr_3/Cs_4PbBr_6$ MCs exhibit a longer lifetime (27.61 ns) than the $CsPbBr_3$ NCs (13.75 nm), suggesting a higher probability of exciton recombination. The wide bandgap of the Cs_4PbBr_6 shell and the abundant halogen atoms on the surface that are in contact with cations give rise to a self-passivation effect by reducing the quantity of surface-trap defect states and nonradiative recombination paths.[53]

Femtosecond transient absorption spectroscopy (fs-TAS) was carried out for the $CsPbBr_3$ and $CsPbBr_3/Cs_4PbBr_6$ QDs to study the ultrafast exciton relaxation and recombination kinetics. Fig. 6a and b show the TA spectra of $CsPbBr_3$ and $CsPbBr_3/Cs_4PbBr_6$ that were measured in the range of 430–600 nm at a pump wavelength of 403 nm and energy of ~4 nJ per pulse at different pump–probe delay times. TA spectra recorded for $CsPbBr_3$ and $CsPbBr_3/Cs_4PbBr_6$ in the range of 430–600 nm spectral window featured (i) a broad positive photoinduced absorption band (PA1, $\Delta A > 0$, where ΔA is change in absorption) in the range of 440–495 nm which is attributed to the forbidden exciton transition activated by the band-edge excitons in strongly quantum confined QDs,[54–56] (ii) different from the PA1, the short lived absorption band (PA2) in the region of 521–560 nm which is assigned to the Stark effect produced by the coulombic interaction between hot carriers and band-edge excitons,[54,56,57] and (iii) a ground state bleach signal (GSB, $\Delta A < 0$), which is sandwiched between two positive absorption bands of two samples at 506 nm for $CsPbBr_3$ and 513 nm for $CsPbBr_3/Cs_4PbBr_6$, matching with the steady state absorption onset, and corresponding to the first exciton absorption peak, which is attributed to the state filling effect of the band edge excitons (depicting the depopulation of ground state) and also a minor contribution from the stimulated emission to GSB signal that cannot be
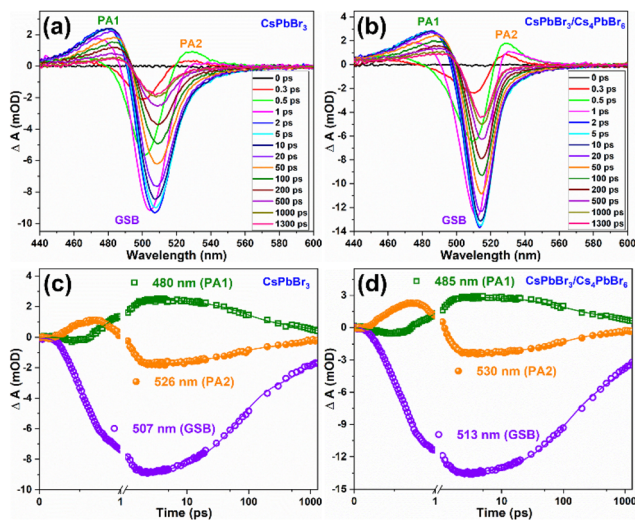
Fig. 6 Femtosecond transient absorption (fs-TA) spectra of (a) CsPbBr₃, (b) CsPbBr₃/Cs₄PbBr₆ measured for various pump–probe delay times at 400 nm excitation, excited-state kinetic curves for the PA1, GSB, and PA2 of (c) CsPbBr₃, (d) CsPbBr₃/Cs₄PbBr₆.

completely ignored.[54,57,58] The negative GBS signals display narrow peaks for two samples due to the localization of the charge carriers, which is also the embodiment of the size uniformity of nanocrystals. The carrier density on the bandgap is explained by the ΔA intensity at the GSB signal. From the TA profiles of two samples, it is also observed that during the initial time delay, the negative GSB signals become increasingly broadened extending over a large range of wavelengths and reaches the maximum at around 2 picoseconds (ps) due to state filling; thereafter with the further increase of delay time, signals gradually narrow down to a symmetric nature displaying a gradual recovery. Therefore, the time required to reach a quasi-thermal distribution of charge carriers in line with the difference between the carrier temperature and lattice temperature (under darkness conditions) causes the bleach signals to broaden during the initial rise in delay time. As can be seen from Fig. 6a and b, the intensity of the bleach signals for CsPbBr₃/Cs₄PbBr₆ is higher than that of CsPbBr₃ under similar experimental conditions including laser intensity, excitation wavelength and delay time. This indicates that Cs₄PbBr₆ can passivate surface states of CsPbBr₃ nanocrystals to eliminate trap fillings.[59] The increase in the intensity of the bleach signal of CsPbBr₃/Cs₄PbBr₆ in contrast to that of CsPbBr₃ is due to the increase in the number of charge carriers in CsPbBr₃ of the CsPbBr₃/Cs₄PbBr₆ core–shell like system.[60] Considering the previous report of J. Xu *et al.*, it is assumed that the CsPbBr₃/Cs₄PbBr₆ dual phase system possesses enhanced oscillator strength in comparison to the pure CsPbBr₃, which favors to achieve intense bleach signal.[61] The GSB trends observed for the CsPbBr₃ and CsPbBr₃/Cs₄PbBr₆ in TA profiles coincide with the previously reported core–shell materials.[59,62–65] The GSB signals in the TA profiles of two samples, exhibited a red shift with an increase of delay time

demonstrating that there exist multiple relaxation paths from the initial excited state after laser excitation.[66–68] The positive absorption bands PA1 and PA2 show a slight red shift in the first few ps due to the exciton–exciton interaction,[66] and the two absorption bands vanish as the delay time increases. Such a trend is because, soon after the completion of intraband cooling, the band edges are populated by the charge carriers, state filling induced bleach dominates the spectra and the carrier-produced stark effect vanishes.[57] The absorption bands PA1 and PA2 reach the maximum at 20 ps and 0.5 ps, respectively, and then gradually decrease. Fig. 6c and d illustrates the TA kinetic curves of PA1, PA2, and GSB at 480, 526, and 507 nm for CsPbBr₃ and 485, 530, and 513 nm for CsPbBr₃/Cs₄PbBr₆ respectively in the delay time range of 0–1300 ps. The decay curves of two samples exhibited a single rise component along with two decay components. The bleach recovery dynamics of the two samples are fitted triexponentially with time constants τ_1 (shorter), τ_2 (longer), and τ_3 (ultra-longer), which contributes to the process of hot-exciton intraband cooling time *i.e.*, intraband relaxation, exciton trapping to the bandgap trap states, and exciton recombination, respectively.[69] $\tau_1 = 0.35$ ps, $\tau_2 = 67.5$ ps, and $\tau_3 = 1.36$ ns for CsPbBr₃ and $\tau_1 = 0.33$ ps, $\tau_2 = 101.4$ ps, and $\tau_3 = 1.57$ ns for CsPbBr₃/Cs₄PbBr₆. The longer exciton lifetimes (ns) for CsPbBr₃/Cs₄PbBr₆ demonstrates that effective passivation of CsPbBr₃ by Cs₄PbBr₆ was accomplished as a result of the reduced surface trap states. Notably, for CsPbBr₃/Cs₄PbBr₆ resembling a core/shell system, hot charge carriers produced by excitation at 403 nm can be delocalized in the conduction band and valence band of both CsPbBr₃ core and Cs₄PbBr₆ shell; as a result both the electrons and holes are depopulated in the CsPbBr₃/Cs₄PbBr₆ system as compared to the pure CsPbBr₃ and finally concentrate into the core, taking extra time. As a result the carrier cooling time in the CsPbBr₃/Cs₄PbBr₆ system was observed to be longer. Due to the difference in the TA kinetic curves, the origin of PA2 is observed to be notably distinct from that of GSB. It is assumed that the formation of polarons by pump excitons could be the origin for PA2.[55,58]

Furthermore, the optical performance of the CsPbBr₃/Cs₄PbBr₆ MCs was explored by measuring the temperature dependence of the steady-state PL spectroscopy measured in the range of 77–300 K. Fig. 7a shows the temperature-dependent PL spectra of the CsPbBr₃/Cs₄PbBr₆ MCs, which display two emission bands at 375 and 528 nm in the UV and green regions, respectively, under 315 nm excitation. The emission band at 375 nm is attributed to the $^3P_1 \rightarrow {}^1S_0$ transition of Pb²⁺ centers in the decoupled [PbBr₆]⁴⁻ octahedral units in Cs₄PbBr₆.[46,70] The intense band in the green region at 528 nm is identical to the green emission of CsPbBr₃, suggesting that the green emission of the Cs₄PbBr₆ MCs is associated with the emission of CsPbBr₃ embedded in the Cs₄PbBr₆ crystal lattice. The position of the green peak at around 528 nm undergoes a blue shift, and its full-width at half-maximum (FWHM) increases with increasing temperature (Fig. S7†). Notably, at low temperatures, the excitons occupy discrete lower-energy levels; as the temperature increases, due to the phonon assist-
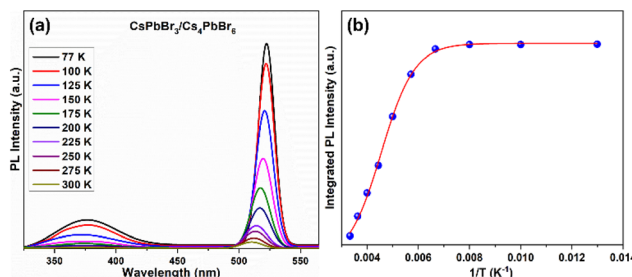
Fig. 7 (a) Temperature-dependent photoluminescence spectra of dual-phase $CsPbBr_3/Cs_4PbBr_6$ MCs measured in the temperature range of 77–300 K under λ_{exci} = 315 nm, and (b) integrated photoluminescence intensity of the green peak as a function of temperature.

ance, the electrons transition from these lower-energy levels to higher ones, which results in the blue shift of the green PL band. The PL intensity of both UV and green bands is quenched with increasing temperature because of the enhanced nonradiative relaxation at a higher temperature. Therefore, to understand the luminescence performance, the nonradiative relaxation process of the $CsPbBr_3/Cs_4PbBr_6$ MCs was investigated by fitting the integrated luminescence of the green emission peak at around 528 nm using the Arrhenius relation:[46,70–72] $I_T = I_0/[1 + A\exp(-E_a/kT)]$, where I_0 is the integrated PL intensity at 0 K, E_a reflects the thermal quenching activation energy, k is the Boltzmann constant, and A is the strength of the thermal quenching process. The integrated PL intensity of $CsPbBr_3/Cs_4PbBr_6$ is plotted as a function of temperature (77–300 K) in Fig. 7b and is well fitted by the above equation. The curve between the integrated PL intensity and the inverse of the temperature evolves to be constant at low temperatures and decreased monotonically with increasing temperature at elevated temperatures. The fit yields an exciton binding energy (BE) of 283.6 ± 32 meV, suggesting that exciton recombination contributes to the intense green emission. The exciton BE of the dual-phase $CsPbBr_3/Cs_4PbBr_6$ MCs (283.6 ± 32 meV) in the present study is higher than previously reported for 3D $CsPbBr_3$ NCs (37–47 meV).[70,73] Due to the lower exciton BE in $CsPbBr_3$, the excitons dissociate into free carriers and travel across the corner-sharing octahedra. In contrast, despite a higher BE, tightly bonded excitons are unlikely to spread through the crystal lattice but are confined in a single unit cell. The higher exciton BE of $CsPbBr_3/Cs_4PbBr_6$ MCs is due to the exciton confinement in the 0D structure within the isolated $[PbBr_6]^{4-}$ octahedral units. Therefore, it is contemplated that the excitons in the $CsPbBr_3/Cs_4PbBr_6$ MCs can be Frenkel excitons rather than Wannier–Mott excitons, and the luminescence process proceeds through exciton recombination in the isolated octahedra.[71,72,74] Under high-energy excitation, the high BE of the green emission suggests that a thermally triggered energy transfer occurs between the Pb^{2+} ions and $[PbBr_6]^{4-}$ octahedra to the green emission centers. We further measured the photoluminescence quantum yield (PLQY) of the $CsPbBr_3$ NCs and dual-phase $CsPbBr_3/Cs_4PbBr_6$ MCs (Fig. S8a and b†). From the PLQY

measurements, we realized that the $CsPbBr_3/Cs_4PbBr_6$ MCs exhibit a remarkable PLQY of 82.7%, which is higher than that of the $CsPbBr_3$ NCs (46.2%). It is speculated that the variation in the PLQY values of both materials can be attributed to the structural arrangement of their $[PbBr_6]^{4-}$ octahedra and Cs^+ cations. It is noteworthy that $CsPbBr_3$ is characterized by corner-sharing $[PbBr_6]^{4-}$ octahedra with Cs^+ cations filling the voids, whereas Cs_4PbBr_6 is characterized by isolated $[PbBr_6]^{4-}$ octahedra, which do not share any corners with Br ions. In the Cs_4PbBr_6 structure, each $[PbBr_6]^{4-}$ octahedron is surrounded by a large number of Cs^+ cations as compared to the $CsPbBr_3$ structure. As a result, Cs_4PbBr_6 is unlikely to be affected by external conditions in the achievement of an efficient exciton PL.[75,76] Moreover, the higher BE and the resulting confined character of the excitons in the isolated octahedra of the Cs_4PbBr_6 matrix are likely to be the reason for the higher PLQY in maintaining structural stability.

Due to such remarkable luminescence properties, dual-phase $CsPbBr_3/Cs_4PbBr_6$ MCs are promising candidates for application in solid-state lighting and display devices. However, their stability against various conditions, including UV light illumination, moisture, and heat, still needs to be explored before they can be used in w-LEDs. The stability of the $CsPbBr_3/Cs_4PbBr_6$ MCs under different conditions was comparably analyzed with that of $CsPbBr_3$ by monitoring their PL intensities at 365 nm excitation. The PL intensities of the dual-phase $CsPbBr_3/Cs_4PbBr_6$ MCs and $CsPbBr_3$ NCs dispersed in toluene as a function of the UV illumination time are compared for a time period of 120 h (Fig. 8a). Under UV illumination, the PL intensities of both samples in toluene exhibited a decreasing trend. The rate at which the PL intensity of $CsPbBr_3/Cs_4PbBr_6$ decreases slowed down after 20 h, whereas the PL intensity of $CsPbBr_3$ NCs gradually decreases at a constant rate. The remnant PL intensities were determined to be 76% for $CsPbBr_3/Cs_4PbBr_6$ and 23% for $CsPbBr_3$. Moisture resistance tests were conducted by storing the pellets of the
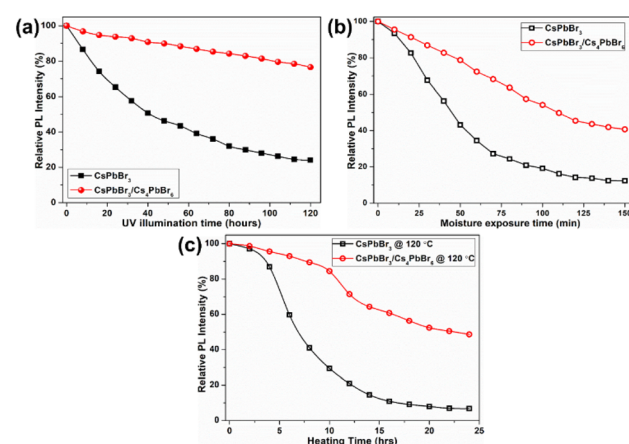
**Fig. 8** (a) UV irradiation test, (b) moisture resistance test, and (c) thermal tolerance test for $CsPbBr_3$ NCs and dual-phase $CsPbBr_3/Cs_4PbBr_6$ MCs conducted by monitoring their emission trends at 365 nm excitation.

$CsPbBr_3/Cs_4PbBr_6$ MCs and $CsPbBr_3$ NCs in an unsealed vial under ambient conditions (at 25 °C, relative humidity of 70%) for a period of time (150 min) (Fig. 8b). The PL intensities of both samples decrease, but the intensity of $CsPbBr_3$ NCs decreases more than that of $CsPbBr_3/Cs_4PbBr_6$ MCs. After 150 min of exposure, the percentage drop in the PL intensities are 42.7% for $CsPbBr_3/Cs_4PbBr_6$ and 12.3% for $CsPbBr_3$. It is well known that perovskite NCs are temperature-sensitive and exhibit relatively poor stability and luminescence quenching, which hinders their practical application. Therefore, thermal tolerance tests were conducted by heating the $CsPbBr_3/Cs_4PbBr_6$ MCs and $CsPbBr_3$ NCs at 120 °C under a 33% ambient condition for 24 hours (Fig. 8c). The PL intensities of both samples decrease slightly during the initial 5 min, but a sudden drop in the intensity of $CsPbBr_3$ is observed afterwards. Meanwhile, a gradual decrease in the PL intensity of $CsPbBr_3/Cs_4PbBr_6$ is observed with increasing heating time. The PL intensity drops faster for $CsPbBr_3$ than for $CsPbBr_3/Cs_4PbBr_6$ under the heat treatment. $CsPbBr_3/Cs_4PbBr_6$ retains 51% of its initial PL intensity after 24 h, whereas the $CsPbBr_3$ retains 8% (Fig. 8c). Subsequently, thermal recovery (luminescence quenching and recovery) tests were conducted by alternating heating and cooling under ambient conditions. The thermal recovery tests involved 10 heating–cooling cycles at two temperatures, 30 °C and 120 °C (Fig. S9a†). The test results reveal that the PL intensity of $CsPbBr_3/Cs_4PbBr_6$ does not decrease after 10 heating–cooling cycles, exhibiting good reversibility. The PL spectra measured between the two temperature points exhibit no change in peak intensity, position, and shape, indicating that the emission from $CsPbBr_3/Cs_4PbBr_6$ is fully reversible (Fig. S9b†).

Based on the excellent optical properties and stability of the as-synthesized green-emitting $CsPbBr_3/Cs_4PbBr_6$ MCs in different environments, their potential application in perovskite-converted w-LEDs for LCD backlighting is demonstrated. As a proof-of-concept experiment, a prototype w-LED was fabricated using a green-emitting $CsPbBr_3/Cs_4PbBr_6$ MCs and a red-emitting $K_2SiF_6:Mn^{4+}$ phosphor (λ_{emi} = 628 nm) combined with a blue-emitting InGaN LED chip (λ_{emi} = 455 nm) as the excitation source to realize white-light emission and achieve a wide color gamut. The $K_2SiF_6:Mn^{4+}$ and $CsPbBr_3/Cs_4PbBr_6$ powders were weighed in different weight ratios (0.05 : 1, 0.3 : 1, 0.6 : 1 and 0.9 : 1) and homogeneously dispersed in polystyrene solution, later drop-cast on a glass slide and then integrated onto the blue-emitting InGaN LED chip (details are provided in the ESI†). The LED devices with the $K_2SiF_6:Mn^{4+}$-to-$CsPbBr_3/Cs_4PbBr_6$ ratios (in wt%) of 0.05 : 1, 0.3 : 1, 0.6 : 1 and 0.9 : 1 are named LED-1, LED-2, LED-3, and LED-4, respectively. Fig. 9a shows the electroluminescence spectra of the fabricated LEDs (LED 1–4) under a 20 mA forward-bias current (2.56 V). The EL spectra of the composite ratio-dependent LEDs (LED 1–4) exhibit three discrete emission bands at 455, 532, and 628 nm, which are attributed to the blue LED chip, green-emitting $CsPbBr_3/Cs_4PbBr_6$, and red-emitting $K_2SiF_6:Mn^{4+}$ powders, respectively. Upon increasing the wt% of the red-emitting component in the composite, the color coor-
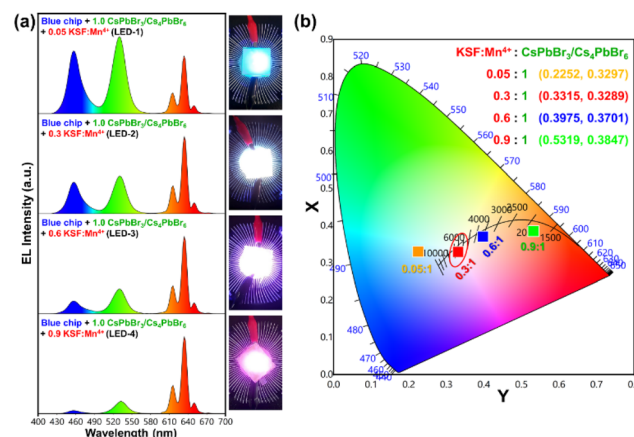

Fig. 9 (a) The electroluminescence spectra of the designed LED devices by varying the $K_2SiF_6:Mn^{4+}$ to $CsPbBr_3/Cs_4PbBr_6$ ratio in the wt% of 0.05 : 1, 0.3 : 1, 0.6 : 1, and 0.9 : 1 under forward-bias current of 20 mA (inset images are photographs of the working LEDs (LED 1–4), (b) the CIE chromaticity coordinates corresponding to the constructed LED devices using different composite wt% ratios.

dinates shift from the cool white-light region to the warm white-light region, corresponding to the correlated color temperature (CCT) decreasing from 12 771 to 1815 K (Fig. 9b and Table S2†). The luminescence efficacy (LE) decreases from 101 lm W^{-1} to 42 lm W^{-1}, and the color rendering index (CRI) tends to increase from 74 to 95 with an increase in the $K_2SiF_6:Mn^{4+}$ ratio in the composite (Table S2†). The reason for such a trend could be that the blue light emitted from the InGaN chip is eventually absorbed by the gradually increasing wt% of the $K_2SiF_6:Mn^{4+}$ phosphor, resulting in a much more intense red emission. The inset images are photographs of the working LEDs (LED 1–4). In the present study, the RGB spectra and wide color gamut space of the LED-2 device were explored by filtering its white-light spectrum using commercial red (R), green (G), and blue (B) color filters (CFs). Using RGB CFs, the color of the displayed objects on the screen is controlled by the transmitted light from the backlight.[77] By varying the ratio between each transmitted RGB CFs, any color of a full-color LCD can be rendered within the color gamut.[78] The transmittance spectra of commercial RGB CFs for LCDs are shown in Fig. 10a. The photographs of unfiltered white light and the RGB filtered white light of the LED-2 device are shown in Fig. 10b. The filtered RGB tricolor spectra of the white-light spectrum emitted from the LED-2 device fabricated using the composite ($K_2SiF_6:Mn^{4+}:CsPbBr_3/Cs_4PbBr_6$ in 0.3 : 1 wt% ratio) and blue LED chip are shown in Fig. 10c. The white and RGB color coordinates of the white-light emitting LED-2 device with CFs under 20 mA operating current are (0.3315, 0.3289), (0.6983, 0.3037), (0.1846, 0.7698), and (0.1442, 0.0749). The obtained white color coordinates (0.3315, 0.3289) are close to those of the standard illumination point D65 (0.3127, 0.3289) and equal energy point (0.333, 0.333) with efficacy of 68 lm W^{-1}, CRI of 87%, and CCT of 5564 K. These results show that this device is a promising candidate for its potential appli-
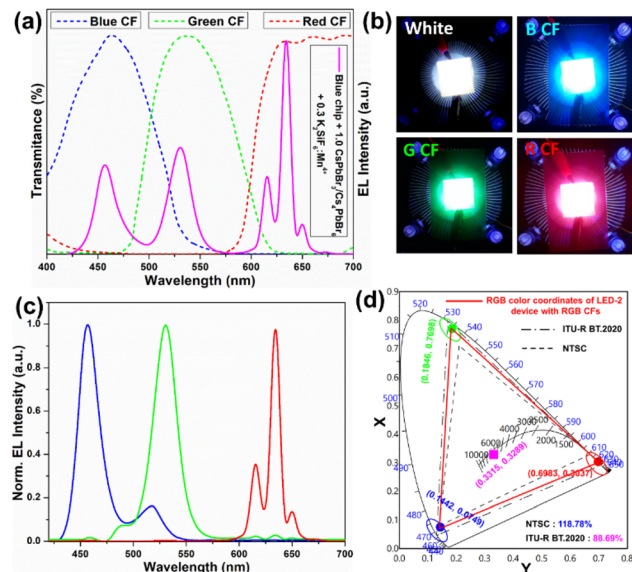
Fig. 10 (a) The transmittance spectra of commercial RGB color filters and unfiltered EL spectrum of a white-light-emitting LED-2 device (K_2SiF_6:Mn^{4+} : $CsPbBr_3$/Cs_4PbBr_6 in 0.3 : 1 wt% ratio), (b) photographs of an unfiltered white-light emitting LED-2 device without CFs and with RGB CFs, (c) filtered RGB EL spectra from white-light emitting LED-2 device (normalized) and (d) CIE color coordinates of filtered RGB EL spectra from a white-light emitting LED-2 device and comparison of the wide color gamut of blue chip + green-emitting $CsPbBr_3$/Cs_4PbBr_6 + red-emitting K_2SiF_6:Mn^{4+} indicated with NTSC standard triangle (−−), and ITU-R BT.2020 triangle (−·−·−).

cation in solid-state lighting and display devices. Based on the filtered RGB color spectra, the LED-2 device achieves a wide color gamut that covers ~118.78% of the National Television Standards Committee (NTSC) and ~88.69% of ITU-R Recommendation BT.2020 (Rec. 2020) triangular spaces in the 1931 CIE diagram, indicated by the red-colored triangle in Fig. 10d. The wide color gamut achieved in this study is very encouraging and considerably better than that of recently reported perovskite-based w-LEDs.[77,78] The details of the photometric and chromaticity parameters of the LED devices under 20 mA forward-bias current are listed in Table S2.† The CIE color coordinates and color gamut of the unfiltered EL spectrum of the white-light emitting LED-2 device are shown in Fig. S10.†

Furthermore, we measured the EL spectra of the optimized LED-2 device at different forward-bias currents (20–200 mA), shown in Fig. S11a,† and it was found that the corresponding color coordinates depend on the operating current. With the increase in the forward-bias current from 20 to 200 mA, the EL intensity enhances, but no change in the shape of the output spectrum occurs, which indicates that the blue light does not saturate the $CsPbBr_3$/Cs_4PbBr_6 luminescence. Additionally, the color coordinates shift from (0.3315, 0.3289) to (0.3047, 0.3611) with an increase in the CCT from 5986 to 6674 K. The LE decreases from 68.2 lm W^{-1} at 20 mA to 14.7 lm W^{-1} at 200 mA. Additionally, the EL spectra were recorded for

different operating time intervals under ambient conditions to examine the stability of the fabricated w-LED operating at 20 mA of current for 10 h under a relative humidity of 70% (Fig. S11b†). No significant change in the shape of the spectra or shift is identified after 10 h. However, with increasing operating time under these conditions, the intensity of the green-emitting $CsPbBr_3$/Cs_4PbBr_6 in the LED-2 device decreases, whereas the blue and red EL bands, which are attributed to the blue LED chip and K_2SiF_6:Mn^{4+}, decrease only slightly. Due to their large-scale production, environmental friendliness, excellent photophysical properties, and strong stability under various environments, the dual-phase $CsPbBr_3$/Cs_4PbBr_6 (core/shell structure) MCs can be a promising green-emitting material in optoelectronic devices.

Conclusions

To summarize, we have successfully synthesized large-scale and ligand-free dual-phase $CsPbBr_3$/Cs_4PbBr_6 rhombohedral MCs using an ultrasonication approach at room temperature. The formation kinetics of the dual-phase $CsPbBr_3$/Cs_4PbBr_6 was investigated at different reaction time intervals (t = 0–30 min). During the synthesis of the dual-phase composite, the $CsPbBr_3$ phase is initially formed in a Pb-rich environment, followed by conversion into the Cs_4PbBr_6 phase when the solution is Cs-rich. Finally, with $CsPbBr_3$ dissolution and Cs_4PbBr_6 crystallization, a dual-phase $CsPbBr_3$/Cs_4PbBr_6 composite is formed exhibiting a high PLQY of 82.7%. The experimental characterization (HR-TEM and PL) provides conclusive evidence for the existence of a small quantity of $CsPbBr_3$ impurities in the Cs_4PbBr_6 MCs, forming a dual-phase $CsPbBr_3$/Cs_4PbBr_6 microstructure, producing strong green emission. The prototype w-LED device fabricated by combining $CsPbBr_3$/Cs_4PbBr_6 and red-emitting K_2SiF_6:Mn^{4+} phosphors onto a blue-emitting InGaN LED chip exhibited a wide color gamut of ~118.78% of the NTSC and ~88.69% of the Rec. 2020. These findings strongly demonstrate that the dual-phase $CsPbBr_3$/Cs_4PbBr_6 (core/shell structure) material can become a green light-emitting material for next-generation solid-state lighting and display applications.

Author contributions

V. Naresh: conceptualization, investigation, methodology, data curation, formal analysis, writing – original draft; Taehyung Jang: transient absorption data curation and analysis; Yoonsoo Pang: resources, writing – review and editing. Nohyun Lee: conceptualization, supervision, project administration, funding acquisition, writing – review and editing.

Conflicts of interest

There are no conflicts to declare.

Acknowledgements

References

1 L. Protesescu, S. Yakunin, M. I. Bodnarchuk, F. Krieg, R. Caputo, C. H. Hendon, R. X. Yang, A. Walsh and M. V. Kovalenko, *Nano Lett.*, 2015, **15**, 3692–3696.

2 F. Chen, M. Imran, L. Pasquale, M. Salerno and M. Prato, *Mater. Res. Bull.*, 2021, **134**, 111107.

3 J. Maes, L. Balcaen, E. Drijvers, Q. Zhao, J. D. Roo, A. Vantomme, F. Vanhaecke, P. Geiregat and Z. Hens, *J. Phys. Chem. Lett.*, 2018, **9**, 3093–3097.

4 W. Zheng, Q. Wan, M. Liu, Q. Zhang, C. Zhang, R. Yan, X. Feng, L. Kong and L. Li, *J. Phys. Chem. C*, 2021, **125**, 3110–3118.

5 S. Ullah, J. Wang, P. Yang, L. Liu, S. E. Yang, T. Xia, H. Guo and Y. Chen, *Mater. Adv.*, 2021, **2**, 646–683.

6 Y. Zhang, R. Sun, X. Ou, K. Fu, Q. Chen, Y. Ding, L. J. Xu, L. Liu, Y. Han, A. V. Malko, X. Liu, H. Yang, O. M. Bakr, H. Liu and O. F. Mohammed, *ACS Nano*, 2019, **13**, 2520–2525.

7 V. Naresh, V. N. K. B. Adusumalli, Y. I. Park and N. Lee, *Mater. Today Chem.*, 2022, **23**, 100752.

8 V. K. Ravi, S. Saikia, S. Yadav, V. V. Nawale and A. Nag, *ACS Energy Lett.*, 2020, **5**, 1794–1796.

9 J. Shi, W. Ge, J. Zhu, M. Saruyama and T. Teranishi, *ACS Appl. Nano Mater.*, 2020, **3**, 7563–7571.

10 H. Chen, R. Li, A. Guo and Y. Xia, *SN Appl. Sci.*, 2021, **3**, 654.

11 X. Liu, X. Zhang, L. Li, J. Xu, S. Yu, X. Gong, J. Zhang and H. Yin, *ACS Appl. Mater. Interfaces*, 2019, **11**, 40923–40931.

12 Q. Zhong, J. Liu, S. Chen, P. Li, J. Chen, W. Guan, Y. Qiu, Y. Xu, M. Cao and Q. Zhang, *Adv. Opt. Mater.*, 2021, **9**, 2001763.

13 P. Kumar, M. Patel, C. Park, H. Han, B. Jeong, H. Kang, R. Patel, W. G. Koh and C. Park, *J. Mater. Chem. B*, 2020, **8**, 10337–10345.

14 V. Naresh, B. H. Kim and N. Lee, *Nano Res.*, 2021, **14**, 1187–1194.

15 X. Pang, S. Si, L. Xie, X. Zhang, H. Huang, S. Liu, W. Xiao, S. Wang, T. Xuan, J. Zhuang, C. Hu, Y. Liu, B. Lei and H. Zhang, *J. Mater. Chem. C*, 2020, **8**, 17374–17382.

16 Q. Wang, W. Wu, R. Wu, S. Yang, Y. Wang, J. Wang, Z. Chai and Q. Han, *J. Colloid Interface Sci.*, 2019, **554**, 133–141.

17 T. Liang, W. Liu, X. Liu, Y. Li, W. Wu and J. Fan, *Chem. Mater.*, 2021, **33**, 4948–4959.

18 J. Zhu, Q. Di, X. Zhao, X. Wu, X. Fan, Q. Li, W. Song and Z. Quan, *Inorg. Chem.*, 2018, **57**, 6206–6209.

19 M. Li, X. Zhang, T. Dong, P. Wang, K. Matras-Postolek and P. Yang, *J. Phys. Chem. C*, 2018, **122**, 28968–28976.

20 Y. Jiang, B. Li, T. Zhang, Y. Shi and Q. H. Xu, *ChemNanoMat*, 2020, **6**, 327–335.

21 J. Shamsi, A. S. Urban, M. Imran, L. De Trizio and L. Manna, *Chem. Rev.*, 2019, **119**, 3296–3348.

22 J. Yin, H. Yang, K. Song, A. M. El-Zohry, Y. Han, O. M. Bakr, J. L. Bredas and O. F. Mohammed, *J. Phys. Chem. Lett.*, 2018, **9**, 5490–5495.

23 L. Wang, H. Liu, Y. Zhang and O. F. Mohammed, *ACS Energy Lett.*, 2020, **5**, 87–99.

24 Q. A. Akkerman, S. Park, E. Radicchi, F. Nunzi, E. Mosconi, F. De Angelis, R. Brescia, P. Rastogi, M. Prato and L. Manna, *Nano Lett.*, 2017, **17**, 1924–1930.

25 L. N. Quan, R. Quintero-Bermudez, O. Voznyy, G. Walters, A. Jain, J. Z. Fan, X. Zheng, Z. Yang and E. H. Sargent, *Adv. Mater.*, 2017, **29**, 1605945.

26 X. Xiong, H. Liu, W. Wang, J. Gong, X. Chen, Y. Zhao, T. Tian and L. Wang, *Luminescence*, 2021, **36**, 631–641.

27 Y. K. Jung, J. Calbo, J. S. Park, L. D. Whalley, S. Kim and A. Walsh, *J. Mater. Chem. A*, 2019, **7**, 20254–20261.

28 M. Hu, C. Ge, J. Yu and J. Feng, *J. Phys. Chem. C*, 2017, **121**, 27053–27058.

29 M. De Bastiani, I. Dursun, Y. Zhang, B. A. Alshankiti, X. H. Miao, J. Yin, E. Yengel, E. Alarousu, B. Turedi, J. M. Almutlaq, M. I. Saidaminov, S. Mitra, I. Gereige, A. AlSaggaf, Y. Zhu, Y. Han, I. S. Roqan, J. L. Bredas, O. F. Mohammed and O. M. Bakr, *Chem. Mater.*, 2017, **29**, 7108–7113.

30 D. Han, H. Shi, W. Ming, C. Zhou, B. Ma, B. Saparov, Y. Z. Ma, S. Chen and M. H. Du, *J. Mater. Chem. C*, 2018, **6**, 6398–6405.

31 Z. Ma, F. Li, D. Zhao, G. Xiao and B. Zou, *CCS Chem.*, 2020, **2**, 71–80.

32 Z. Qin, S. Dai, V. G. Hadjiev, C. Wang, L. Xie, Y. Ni, C. Wu, G. Yang, S. Chen, L. Deng, Q. Yu, G. Feng, Z. M. Wang and J. Bao, *Chem. Mater.*, 2019, **31**, 9098–9104.

33 N. Riesen, M. Lockrey, K. Badek and H. Riesen, *Nanoscale*, 2019, **11**, 3925–3932.

34 X. Chen, F. Zhang, Y. Ge, L. Shi, S. Huang, J. Tang, Z. Lv, L. Zhang, B. Zou and H. Zhong, *Adv. Funct. Mater.*, 2018, **28**, 1706567.

35 L. Rao, Y. Tang, C. Song, K. Xu, E. T. Vickers, S. B. Naghadeh, X. Ding, Z. Li and J. Z. Zhang, *Chem. Mater.*, 2019, **31**, 365–375.

36 J. Shamsi, A. S. Urban, M. Imran, L. De Trizio and L. Manna, *Chem. Rev.*, 2019, **119**, 3296–3348.

37 L. Rao, X. Ding, X. Du, G. Liang, Y. Tang, K. Tang and J. Z. Zhang, *J. Nanotechnol.*, 2019, **10**, 666–676.

38 A. Moghtada and R. Ashiri, *Ultrason. Sonochem.*, 2016, **33**, 141–149.

39 G. Hu, W. Qin, M. Liu, X. Ren, X. Wu, L. Yang and S. Yin, *J. Mater. Chem. C*, 2019, **7**, 4733.

40 T. Xuan, S. Lou, J. Huang, L. Cao, X. Yang, H. Li and J. Wang, *Nanoscale*, 2018, **10**, 9840.

41 S. Cho and S. H. Yun, *Commun. Chem.*, 2020, **3**, 15.

42 Y. Li, W. Shao, L. Chen, J. Wang, J. Nie, H. Zhang, S. Zhang, R. Gao, X. Ouyang, X. Ouyang and Q. Xu, *NPG Asia Mater.*, 2021, **13**, 40.

43 Q. Xu, J. Wang, W. Shao, X. Ouyang, X. Wang, X. Zhang, Y. Guo and X. Ouyang, *Nanoscale*, 2020, **12**, 9727–9732.

44 W. Wang, Y. Wu, D. Wang and T. Zhang, *ACS Omega*, 2019, **4**, 19641–19646.

45 W. Wang, D. Wang, F. Fang, S. Wang, G. Xu and T. Zhang, *Cryst. Growth Des.*, 2018, **18**, 6133–6141.

46 J. Yin, Y. Zhang, A. Bruno, C. Soci, O. M. Bakr, J. L. Bredas and O. F. Mohammed, *ACS Energy Lett.*, 2017, **2**, 2805–2811.

47 Z.-P. Huang, B. Ma, H. WanFg, N. Li, R.-T. Liu, Z.-Q. Zhang, X.-D. Zhang, J.-H. Zhao, P.-Z. Zheng, Q. Wang and H.-L. Zhang, *J. Phys. Chem. Lett.*, 2020, **11**, 6007–6015.

48 Y. Li, X. Yang and A. Xie, *J. Lumin.*, 2021, **236**, 118154.

49 T. Liang, W. Liu, X. Liu, Y. Li, W. Wu and J. Fan, *Chem. Mater.*, 2021, **33**, 4948–4959.

50 P. Reiss, M. Protiere and L. Li, *Small*, 2009, **5**, 154–168.

51 Q. A. Akkerman, A. L. Abdelhady and L. Manna, *J. Phys. Chem. Lett.*, 2018, **9**, 2326–2337.

52 F. Cao, D. Yu, X. Xu, Z. Han and H. Zeng, *J. Phys. Chem. C*, 2021, **125**, 3–19.

53 X. Li, Y. Wu, S. Zhang, B. Cai, Y. Gu, J. Song and H. Zeng, *Adv. Funct. Mater.*, 2016, **26**, 2435–2445.

54 N. Mondal, A. De, S. Das, S. Paul and A. Samanta, *Nanoscale*, 2019, **11**, 9796–9818.

55 N. Mondal and A. Samanta, *Nanoscale*, 2017, **9**, 1878–1885.

56 B. R. C. Vale, E. Socie, A. B. Caminal, J. Bettini, M. A. Schiavon and J.-E. Moser, *J. Phys. Chem. Lett.*, 2020, **11**, 387–394.

57 G. Kaur, K. J. Babu, N. Ghorai, T. Goswami, S. Maiti and H. N. Ghosh, *J. Phys. Chem. Lett.*, 2019, **10**, 5302–5311.

58 C. Qin, Z. Jiang, Z. Zhou, Y. Liu and Y. Jiang, *Nanotechnology*, 2021, **32**, 455702.

59 J.-F. Liao, Y.-F. Xu, X.-D. Wang, H.-Y. Chen and D.-B. Kuang, *ACS Appl. Mater. Interfaces*, 2018, **10**, 42301–42309.

60 J. Dana, P. Maity, B. Jana, S. Maiti and H. N. Ghosh, *ACS Omega*, 2018, **3**, 2706–2714.

61 J. Xu, W. Huang, P. Li, D. R. Onken, C. Dun, Y. Guo, K. B. Ucer, C. Lu, H. Wang, S. M. Geyer, R. T. Williams and D. L. Carroll, *Adv. Mater.*, 2017, **29**, 1703703.

62 G. Kaur, K. J. Babu, N. Ghorai, T. Goswami, S. Maiti and H. N. Ghosh, *J. Phys. Chem. Lett.*, 2019, **10**, 5302–5311.

63 J. Yin, P. Maity, M. De Bastiani, I. Dursun, O. M. Bakr, J. L. Bredas and O. F. Mohammed, *Sci. Adv.*, 2017, **3**(12), e1701793.

64 V. Gray, P. Xia, Z. Huang, E. Moses, A. Fast, D. A. Fishman, V. I. Vullev, M. Abrahamsson, K. M. Poulsen and M. L. Tang, *Chem. Sci.*, 2017, **8**, 5488–5496.

65 Y. Wu, C. Wei, X. Li, Y. Li, S. Qiu, W. Shen, B. Cai, Z. Sun, D. Yang, Z. Deng and H. Zeng, *ACS Energy Lett.*, 2018, **3**, 2030–2037.

66 J. Xu, L. Zhu, J. Chen, S. Riaz, L. Sun, Y. Wang, W. Wang and J. Dai, *Phys. Status Solidi RRL*, 2021, **15**, 2000498.

67 X. Shen, S. Wang, C. Geng, L. Li, E. Zhao, J. Sun, W. Wu, L. An and K. Pan, *J. Phys. Chem. C*, 2021, **125**, 5278–5287.

68 L. Wu, M. Zhang, S. Yang, R. Wu, S. Gong, Q. Han and W. Wu, *J. Alloys Compd.*, 2021, **889**, 161721.

69 J.-S. Yao, J. Ge, B.-N. Han, K.-H. Wang, H.-B. Yao, H.-L. Yu, J.-H. Li, B.-S. Zhu, J.- Z. Song, C. Chen, Q. Zhang, H.-B. Zeng, Y. Luo and S.-H. Yu, *J. Am. Chem. Soc.*, 2018, **140**, 3626–3634.

70 Z. Bao, Y. J. Tseng, W. You, W. Zheng, X. Chen, S. Mahlik, A. Lazarowska, T. Lesniewski, M. Grinberg, C. Ma, W. Sun, W. Zhou, R. S. Liu and J. P. Attfield, *J. Phys. Chem. Lett.*, 2020, **11**, 7637–7642.

71 Y. Zhang, M. I. Saidaminov, I. Dursun, H. Yang, B. Murali, E. Alarousu, E. Yengel, B. A. Alshankiti, O. M. Bakr and O. F. Mohammed, *J. Phys. Chem. Lett.*, 2017, **8**, 961–965.

72 H. Yang, Y. Zhang, J. Pan, J. Yin, O. M. Bakr and O. F. Mohammed, *Chem. Mater.*, 2017, **29**, 8978–8982.

73 B. T. Diroll, H. Zhou and R. D. Schaller, *Adv. Funct. Mater.*, 2018, **28**, 1800945.

74 H. Zhang, Q. Liao, Y. Wu, J. Chen, Q. Gao and H. Fu, *Phys. Chem. Chem. Phys.*, 2017, **19**, 29092–29098.

75 M. I. Saidaminov, J. Almutlaq, S. Sarmah, I. Dursun, A. A. Zhumekenov, R. Begum, J. Pan, N. Cho, O. F. Mohammed and O. M. Bakr, *ACS Energy Lett.*, 2016, **1**, 840–845.

76 D. Chen, Z. Wan, X. Chen, Y. Yuan and J. Zhong, *J. Mater. Chem. C*, 2016, **4**, 10646–10653.

77 Z. Luo, Y. Chen and S. T. Wu, *Opt. Express*, 2013, **21**, 26269–26284.

78 H. C. Yoon, S. Lee, J. K. Song, H. Yang and Y. R. Do, *ACS Appl. Mater. Interfaces*, 2018, **10**, 11756–11767.